Increasing the Collision Rate of Particle Impact Electroanalysis with Magnetically Guided Pt-Decorated Iron Oxide Nanoparticles

Donald A. Robinson, Jason J. Yoo, Alma D. Castañeda, Brett Gu, Radhika Dasari, Richard M. Crooks, and Keith J. Stevenson*

Department of Chemistry, Center for Nano- and Molecular Science and Technology, Texas Materials Institute, and Center for Electrochemistry, The University of Texas at Austin, Austin, Texas 78712, United States

ABSTRACT An integrated microfluidic/magnetophoretic methodology was developed for improving signal response time and detection limits for the chronoamperometric observation of discrete nanoparticle/electrode interactions by electrocatalytic amplification. The strategy relied on Pt-decorated iron oxide nanoparticles which exhibit both superparamagnetism and electrocatalytic activity for the oxidation of hydrazine. A wet chemical synthetic approach succeeded in the controlled growth of Pt on the surface of FeO/Fe_3O_4 core/shell nanocubes, resulting in highly uniform Pt-decorated iron oxide hybrid nanoparticles with good dispersibility in water. The unique mechanism of hybrid nanoparticle formation was investigated by electron microscopy and spectroscopic analysis of isolated nanoparticle intermediates and final products. Discrete hybrid nanoparticle collision events were detected in the presence of hydrazine, an electrochemical indicator probe, using a gold microband electrode integrated into a microfluidic channel. In contrast with related systems, the experimental nanoparticle/electrode collision rate correlates more closely with simple theoretical approximations, primarily due to the accuracy of the nanoparticle tracking analysis method used to quantify nanoparticle concentrations and diffusion coefficients. Further modification of the microfluidic device was made by applying a tightly focused magnetic field to the detection volume to attract the magnetic nanoprobes to the microband working electrode, thereby resulting in a 6-fold increase to the relative frequency of chronoamperometric signals corresponding to discrete nanoparticle impact events.

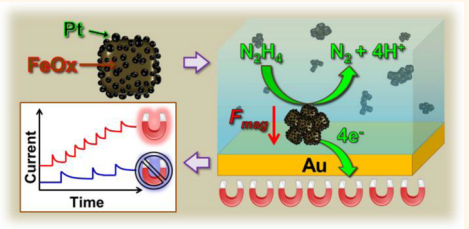

KEYWORDS: nanoparticle collisions · electrocatalytic amplification · multifunctional nanoparticles · hybrid nanoparticles · microfluidics · magnetophoresis

Recent coevolutionary progress in the colloidal synthesis and characterization of inorganic nanoparticles (NPs) has enabled researchers to recognize, understand, and tailor certain properties of interest in order to produce specialized NPs that can be employed to perform one or more important functions for a target application. The degree of multifunctionality can be further increased by interfacing two or more different inorganic nanomaterials together into one nanostructure, a so-called hybrid nanoparticle.[1] Herein, we demonstrate that specially designed colloidal magnetic/catalytic hybrid NPs, each composed of a superparamagnetic iron oxide nanoparticle (IONP) core densely decorated with smaller Pt NPs embedded on the surface, are particularly useful bifunctional nanoscale probes for the development of a novel microfluidic sensing platform that integrates electrocatalytic amplification[2] of individual NP/electrode collisions with magnetic NP actuation.[3]

IONPs have received considerable attention as their intrinsic magnetic properties can be exploited for a variety of functions, predominantly those pertaining to biomedical science and technology.[4,5] One specific property of interest is IONP magnetization by applying an external magnetic field, which results in exertion of a translational magnetophoretic force on the suspended IONP.[6] This is a highly desirable asset for applications that can benefit from controlled magnetophoresis of NPs,[7−10] including

* Address correspondence to stevenson@cm.utexas.edu.

Received for review May 12, 2015 and accepted July 13, 2015.

Published online July 13, 2015
10.1021/acsnano.5b02892

microfluidic lab-on-a-chip sensors.[3,11] Biofunctionalized magnetic NPs or microbeads can be integrated into various microfluidic sensing platforms to serve as target capture agents, which are then subsequently manipulated by an external magnetic field to isolate, concentrate, and/or rapidly transport the target molecules to the detection volume or surface. This fundamental strategy of integrating magnetic particle actuation[3] with microfluidic devices has been demonstrated to significantly reduce analysis times and limits of detection in nucleic acid assays and immunoassays.[3,11]

Pt NPs are generally renowned for their exceptional activity and versatility in heterogeneous catalysis.[12] This quality has inspired the development of electrochemical affinity biosensor methodologies[13] that incorporate Pt NP labels for electrocatalytically amplified response.[14−19] A great advantage of using colloidal Pt NPs as sensing labels is that they can be detected individually from aqueous suspension by particle impact electroanalysis.[20−23] Xiao and Bard first reported the chronoamperometric (CA) detection of discrete Pt NP impact events with an ultramicroelectrode (UME) by electrocatalytic amplification (EA).[24] Since then, the most popular and well-studied system for detecting individual NP/electrode impacts by EA (*a.k.a.* EA collisions) has relied on Pt NPs as the nanocatalysts and hydrazine oxidation as the electrochemical indicator reaction.[18,25−35] Crooks and co-workers recently showed that this methodology could be adopted to detect individual DNA hybridization events in a microfluidic electrochemical cell,[18] thus demonstrating single-molecule level sensitivity with a bioassay based on NP impact electrochemistry.

While the sensitivity of the aforementioned detection platform is very impressive, the lowest concentration of analyte that can be detected in a reasonable amount of time is severely limited by diffusive NP transport. Considering the NP impact system without any DNA modification, the frequency of detected NP collisions is dependent not only on the bulk NP concentration but also NP mass transport kinetics, which are primarily controlled by diffusion (with some convective contribution in the case of microfluidic channels where the solution flows orthogonal to the plane of the microelectrode surface).[34] The major inherent drawback in the method is that the working electrode must be kept at microscale dimensions in order to detect a single NP collision event with adequate signal-to-noise (S/N). This is necessary to keep the background noise low (subpicoampere) so that the CA signal (picoamperes) corresponding to a NP collision event is discernible. The reliance on slow diffusive NP transport to a microscale detection area sets a relatively high limit of detection (LOD) that has been reported to range from 10^{-14} to 10^{-11} M Pt NPs, depending on experimental conditions, colloidal size distributions, and the accuracy of the method for which NP concentrations are quantified.[25−34]

To increase the relative collision rate and improve the LOD of single particle collision-based detection methods, we developed a strategy to apply a focused magnetic field to drive magnetophoretic migration of probe NPs to the microelectrode. It should be noted that the combination of magnetic field manipulation and particle impact electroanalysis has been recently investigated by us and other groups,[36−39] the most relevant of which is that of Crooks and co-workers, who recently reported particle impact electroanalysis of insulating magnetic microbeads in a microfluidic channel detected by the blockage of redox indicator flux to the microband electrode.[39] Furthermore, we described a magnetic enrichment method using a sliding permanent magnet to preconcentrate the magnetic beads toward the microband electrode, which allowed for subattomolar detection of the microbeads (2.82 μm avg. diameter).

Some aspects of the approach reported here are similar to those described in our earlier report,[39] but there are key differences. First, we rely here on EA, so the NPs are much smaller than in our previous report. Such NPs are more desirable to achieve ultrahigh sensitivity in affinity-based bioassays. Second, we also report an optimized synthetic protocol to achieve hybrid Pt-IONPs with good colloidal stability in physiological buffer systems, along with supplemental mechanistic insight into the synthesis. Integration of the magnetic function (to increase collision frequency) with the electrocatalytic signaling function in a single NP provides a viable format for low-level, and perhaps single molecule, biosensing. Third, we used NP tracking analysis (NTA) to measure the NP diffusion coefficients and concentrations used in EA collision experiments, thereby providing a more accurate quantification of NP collision rate compared to previously reported methods.[25−34] The resulting collision rate was found to correlate much more closely to theoretical predictions than preceding reports relying on Pt colloids in the presence of the hydrazine indicator.[25−34]

RESULTS AND DISCUSSION

Synthesis and Surface Modification of IONPs. The aqueous synthesis of hybrid Pt-IONPs is outlined in Scheme 1, beginning with core/shell wüstite/magnetite nanocubes that were synthesized using a modified version of the iron(III) oleate decomposition method reported by Hai *et al.*[40] As shown in Figure S1 of the Supporting Information, the powder X-ray diffraction (XRD) pattern of the IONPs contains diffraction angles/intensities corresponding to both magnetite (Fe_3O_4) spinel and wüstite ($Fe_{1-x}O$) rock salt crystallites.[41] The presence of $Fe_{1-x}O$ phase contained within the interior of the nanocubes is evidenced by the varied degrees of contrast observed by scanning transmission electron

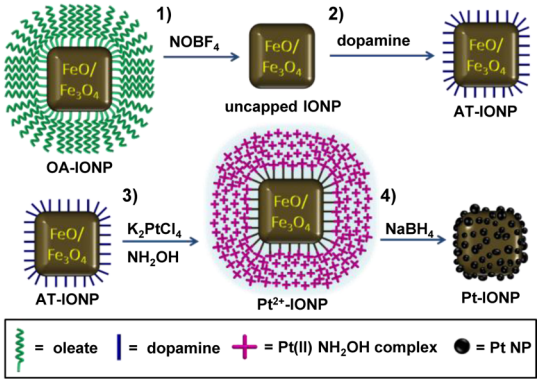

Scheme 1. Synthesis of Pt-IONPs.

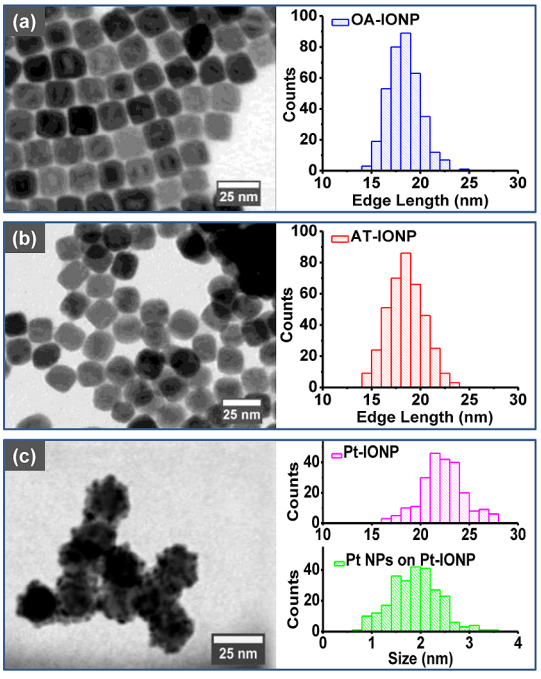

Figure 1. STEM images and corresponding size histograms for (a) OA-IONP, (b) AT-IONP, and (c) Pt-IONP. Included in (c) is the size distribution for the attached Pt domains on Pt-IONP.

microscopy (STEM) (Figure 1a,b). Comparable XRD characteristics and electron micrographs have been reported in previous characterizations of $Fe_{1-x}O/Fe_3O_4$ core/shell nanoparticles.[40,42−47]

The first step of the Pt-IONP synthesis involves the removal of capping ligands by reacting the oleate-capped iron oxide nanoparticles (OA-IONPs) with nitrosonium tetrafluoroborate salt ($NOBF_4$).[48] The resulting "naked" IONPs form excellent dispersions in polar organic solvents such as *N*,*N*-dimethylformamide, but have limited stability in aqueous solutions.[48] To improve their dispersibility in water and terminate the iron oxide surface with amine functional groups, a second step was implemented to produce amine-terminated iron oxide nanoparticles (AT-IONPs) by the surface modification of "naked" IONPs with dopamine. The dopamine ligand preferentially binds to the iron oxide surface *via* the coordination of its chelating catechol functional group,[49] which renders the IONPs more hydrophilic and promotes further modification by providing exposed amine groups on the NP surface.[50] The ligand removal procedure and subsequent dopamine surface modification do not appear to significantly affect the size distribution of the iron oxide nanocrystals, as the resulting AT-IONPs remain 18 (±2) nm in size and cubic in shape (Figure 1a,b).

Characterization of Pt^{2+}-Coated Intermediate. Steps 3 and 4 of Scheme 1 were developed based on our previous work.[51] In step 3, the terminal amine groups serve as ligands to bind Pt^{2+} to the IONP surface by ligand exchange with $[PtCl_4]^{2-}$ to form square planar Pt^{2+} amine complexes. Subsequent addition of hydroxylamine (NH_2OH) produces an additional species of Pt^{2+} amine complexes, which have the effect of agglomerating around the IONP to form a thin coating over its surface after sonication at 60 °C for 2 h. The resulting Pt^{2+}-coated iron oxide NPs (Pt^{2+}-IONPs) can be rinsed several times with aqueous solutions of pH 5−12 without dissolving the Pt^{2+} ions, demonstrating the remarkable stability of the NH_2OH-ligated Pt^{2+} complexes and the interactions keeping them adhered to the IONPs. The role of NH_2OH in noble metal NP synthesis is usually to act as a reducing agent. Such is the case for the synthesis of Au,[52−54] Ag,[55] and Pd NPs.[56] For Pt, however, NH_2OH does not act as a reducing agent at neutral pH, but rather coordinates as a ligand in a fashion analogous to ammonia to produce a series of relatively stable platinum salt compounds.[57−59]

The results of X-ray photoelectron spectroscopy (XPS) in the Pt 4f region of the intermediate formed in step 3 confirm that the majority of Pt species remains as Pt^{2+} (Figure 2, top panel). The only diffraction peaks observed by powder XRD of the Pt^{2+}-IONP intermediate are those corresponding to $Fe_{1-x}O$ and Fe_3O_4, which indicates that the Pt^{2+} coating is amorphous (Supporting Information Figure S1). The thin Pt^{2+} coating was observed to nucleate small Pt^0 nanoparticles on the Fe_3O_4 surface during characterization by electron microscopy due to the reducing power of the electron beam.[60] A time-lapsed TEM video was recorded to capture the transformation from an amorphous coating over the IONPs to a densely packed monolayer of embedded Pt NPs (Supporting Information video). As shown by the STEM image in Figure S2d of Supporting Information, the cubic morphology of the IONP cores was preserved underneath their Pt NP shells.

A series of control reactions were carried out for step 3 to gain some mechanistic insight into the formation of the Pt^{2+}-IONP intermediate. All synthetic conditions were kept consistent while omitting the preceding dopamine modification of IONPs, the

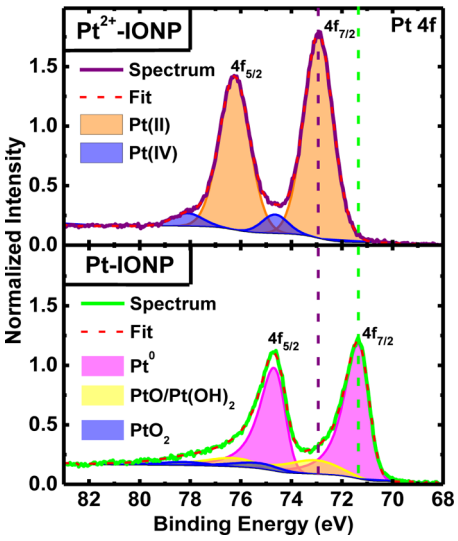

Figure 2. Fitted Pt 4f XP spectra for Pt^{2+}-IONP intermediate (top panel) and Pt-IONP final product (bottom panel). Spectra intensities were normalized by corresponding Fe $2p_{3/2}$ peak maximum. Vertical dashed lines indicate Pt $4f_{7/2}$ peak position.

addition of NH_2OH, or both (Supporting Information Figure S2). If naked IONPs are reacted directly with K_2PtCl_4 precursor by sonication at 60 °C, the synthesis results in the premature reduction of Pt^{2+} to Pt^0, yielding polydisperse dendritic Pt nanostructures unevenly distributed throughout the sample (Supporting Information Figure S2a). The structural integrity of the IONP precursor appears to be significantly compromised after this reaction, which may be due to oxidation, partial dissolution, and/or restructuring of the IONPs resulting from galvanic exchange between Pt^{2+} and Fe^{2+} of the mixed valence unprotected iron oxide NPs. If the same reaction is carried out in the presence of NH_2OH, the adsorbed Pt remained in its unreduced Pt^{2+} state (Supporting Information Figure S2b). As shown in Supporting Information Figure S2c, a similar result was observed after reacting AT-IONPs directly with K_2PtCl_4 in the absence of NH_2OH, except with less Pt^{2+} adsorbed. Both NH_2OH and catechol-anchored dopamine evidently act as inhibitors to the electrochemical reduction of Pt^{2+}, possibly owing to the high stability of their respective Pt^{2+} complexes in comparison to $PtCl_4^{2-}$. The use of both AT-IONPs (instead of naked IONPs) and NH_2OH in the synthesis led to the highest accumulation of adsorbed Pt^{2+} species uniformly coating the iron oxide nanocubes, as evidenced by energy dispersive X-ray spectroscopy (EDX) and STEM (Supporting Information Figure S2d).

Further XPS analysis was performed to investigate the change in elemental composition, starting from the AT-IONP precursor and ending with the Pt-IONP final product. The XPS data and quantitative summary are shown in Figures S3 and S4 of Supporting Information, respectively. The atomic ratio of O to Fe is 1.47 for the AT-IONP precursor, suggesting that the IONP surface is

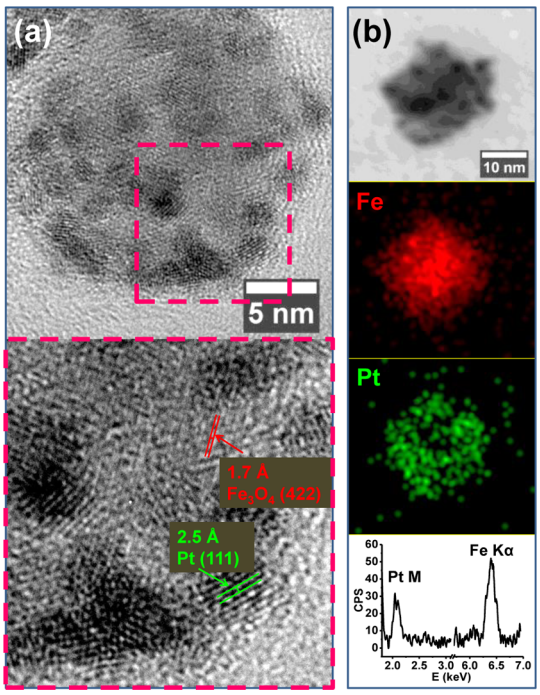

Figure 3. (a) HR-TEM of single Pt-IONP with zoomed in view on lower panel showing Pt and Fe_3O_4 lattice fringes labeled with interplanar lattice spacing. (b) STEM of single Pt-IONP with EDX elemental mapping and corresponding spectrum.

terminated with both Fe_3O_4 and Fe_2O_3. A 7-fold supplement to the relative composition of nitrogen was found to result from the reaction in step 3. The chemical composition of the Pt^{2+}–NH_2OH complexes of the Pt^{2+}-IONP intermediate remains unclear, but quantitative XPS analysis results in a N:O:Pt atomic ratio of 2:2:1, which is consistent with the findings of our previous report[51] and suggests a stoichiometric ratio of two NH_2OH ligands per one Pt^{2+} coordination center. The Cl distribution observed by XPS was found to vary relatively little in comparison to N and O, indicating that Cl only makes a minor contribution (Cl:Pt ~ 0.3:1) to the composition of the adsorbed Pt^{2+} complexes. Therefore, we propose that the Pt^{2+} coating over the MNP surfaces is primarily composed of $[Pt(NH_2OH)_2Cl_x(H_2O)_y(OH)_z]^n$ complex species that are linked together by intermolecular hydrogen bonding, electrostatic interactions, and/or by intermolecular cross-linking of the ambidentate NH_2OH ligand.

Structural Characterization of Pt-IONP Product. Reacting the purified Pt^{2+}-MNP intermediate with $NaBH_4$ reduces Pt^{2+} to Pt^0 and triggers formation of small Pt NPs (~2 nm) that decorate the iron oxide surface (Figure 1c). The interplanar lattice spacings for Fe_3O_4 (422) and Pt (111) planes are observed through HR-TEM imaging of the lighter and darker contrast regions of the particle, respectively (Figure 3a). The EDX spectrum of a single Pt-IONP is shown in Figure 3b along with corresponding elemental mapping of Fe and Pt, which confirms that the Pt-IONP is composed of an iron oxide

core supporting several Pt NPs that densely cover its surface. Powder XRD of the Pt-IONP sample reveals a very broad peak corresponding to the diffraction angle of Pt(111) (Supporting Information Figure S1). The average diameter of the Pt crystallite domains was estimated to be approximately 2 nm using the Scherrer formula,[61] which provides good agreement with TEM sizing in Figure 1c.

The Pt 4f XP spectrum for Pt-IONP is shown in the bottom panel of Figure 2. The $4f_{7/2}$ core electron binding energy for Pt^0 of the Pt-IONP sample is 71.2 eV, which is the typical value for bulk Pt.[62] This result was unexpected, however, considering the strong metal–support interactions that were previously observed for Pt–Fe_3O_4 hybrid NPs, as evidenced by a significant shift of the Pt^0 $4f_{7/2}$ core electron binding energy to a lower value (70.6–70.8 eV).[51,63,64] This XPS spectral shift was ascribed to a charge transfer from the Fe_3O_4 to the Pt domains, thus electronically enriching the Pt atoms and screening the effective nuclear charge to result in a shift to lower core electron binding energy. In our previous work, dopamine was not used to modify IONPs before platinum deposition. Instead, IONPs were synthesized with 1,6-hexanediamine as the capping agent.[51] In the current system, the amine functionalizing species (dopamine) is likely to undergo substantial polymerization under the slightly alkaline reaction conditions[65,66] and encapsulate the IONPs with a polydopamine coating.[67,68] The polydopamine layer may separate the Fe_3O_4 surface of the IONPs from the decorating Pt NPs, thus preventing interfacial charge transfer. This is just one possible explanation for why a core electron shift to lower binding energy was not observed. Further rigorous microstructural characterization is necessary to fully elucidate the metal–support interactions of Pt-IONPs.[69]

Catalytic and Magnetic Characterization of Pt-IONPs. The electrocatalytic activity of Pt-IONPs for the hydrazine oxidation reaction in pH 7.5 phosphate buffer was qualitatively investigated by performing cyclic voltammetry (CV) on carbon-supported Pt-IONP (Pt-IONP/C) thin films deposited on glassy carbon working electrode (Figure 4a). For the case of the platinum-free AT-IONP/C film, no appreciable electrocatalytic anodic current is generated until the potential is swept positive of 0 V *vs* Ag/AgCl. In contrast, the current associated with hydrazine oxidation on hybrid Pt-IONPs is apparent at approximately −0.45 V *vs* Ag/AgCl, which is a slightly more negative potential than that observed for a Pt UME (Figure 4b). Rotating disk linear sweep voltammetry (LSV) was performed at various rotation speeds to determine the kinetic current (i_K) associated with electrocatalytic oxidation of N_2H_4 at the Pt-IONP/C catalyst film at 0 V *vs* Ag/AgCl (Supporting Information Figure S5a). The corresponding Koutecky–Levich plot shown in Supporting Information Figure S5b was

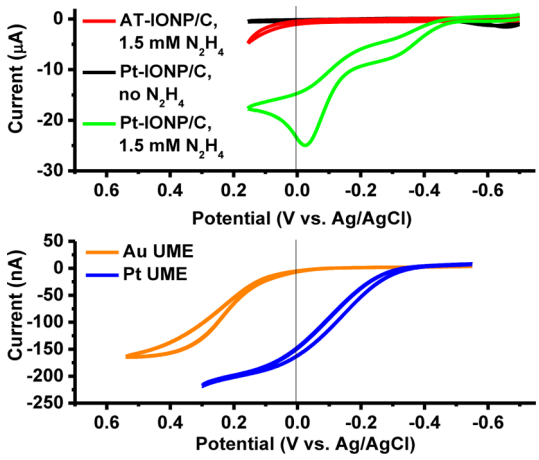

Figure 4. Cyclic voltammograms for oxidation of hydrazine in 50.0 mM sodium phosphate buffer at pH 7.5 on (a) carbon-supported AT-IONP and Pt-IONP catalyst films on glassy carbon electrode, 1.5 mM hydrazine (red and green lines), no hydrazine (black line), 5 mV/s scan rate and (b) Au and Pt UMEs, 15.0 mM hydrazine, 50 mV/s scan rate. Vertical lines at 0 V *vs* Ag/AgCl designate the potential applied in chronoamperometric NP collision experiments.

constructed to extrapolate a value for i_K (0.509 mA). The Pt electroactive surface area (ECSA) of the Pt-IONP/C catalyst film was estimated from anodic CO stripping voltammetry (Supporting Information Figure S5c,d). CO stripping voltammetry in alkaline conditions was chosen over hydride adsorption/desorption for determining Pt ECSA because the iron oxide portion of Pt-IONPs readily dissolves in strong acidic media. As shown in Supporting Information Figure S5c, before any exposure to CO, the cyclic voltammogram of the Pt-IONP/C film presents one anodic peak at −0.1 V (*vs* $Hg/HgSO_4$) and one cathodic peak at −0.3 V, both corresponding to the Fe^{2+}/Fe^{3+} redox couple of iron oxide. After exposure to CO and subsequent purging of excess CO with N_2 bubbling, an increase in current is apparent at −0.2 V. The current associated with the Fe^{2+}/Fe^{3+} anodic peak was subsequently subtracted from the one acquired after CO exposure to isolate the current corresponding to adsorbed CO oxidation (Supporting Information Figure S5d). Pt ECSA was calculated based on the charge from the integral of the peak area with respect to time and the specific charge (420 $\mu C/cm^2$) for a monolayer of adsorbed CO. Pt surface specific activity was calculated to be 34.9 mA/cm^2 of exposed Pt in the presence of 1.5 mM N_2H_4 in 50 mM sodium phosphate buffer (pH 7.5).

The magnetic properties of AT-IONPs and Pt-IONPs were characterized by vibrating sample magnetometry (VSM). As shown in Figure 5, the saturation magnetization (M_s) of the AT-IONP sample (116 emu/g Fe) is relatively high compared to that of core/shell $Fe_{1-x}O/Fe_3O_4$ NPs of similar size[40,45] and approaches the M_s of bulk Fe_3O_4 (92 emu/g Fe_3O_4 or 128 emu/g Fe).[70] The magnetization is substantially lower for Pt-IONPs (M_s = 39 emu/g Fe), which indicates a magnetic shielding

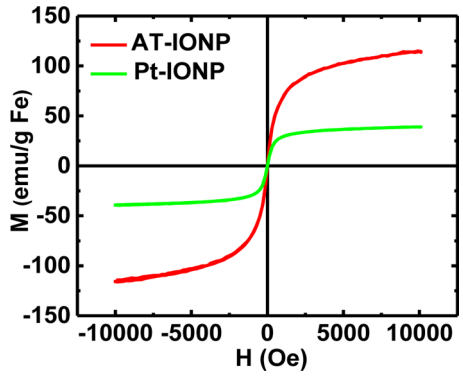

Figure 5. Magnetization curves with respect to applied magnetic field from room temperature VSM of AT-IONPs and Pt-IONPs.

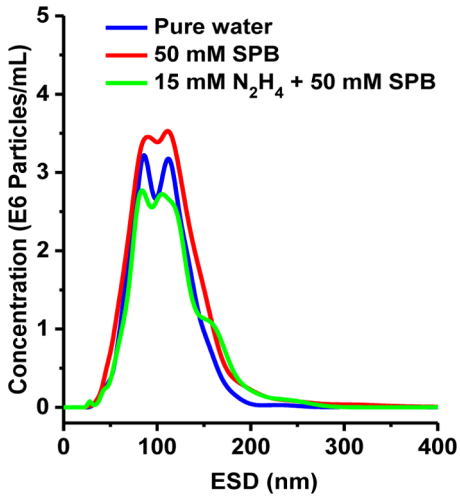

Figure 6. Pt-IONP hydrodynamic size distributions under different solution conditions. All samples were prepared by 100-fold dilution of an aqueous stock Pt-IONP suspension using either pure water, 50.0 mM SPB, or 15.0 mM N_2H_4 + 50.0 mM SPB as the diluents.

effect contributed by the dense layer of Pt NPs covering each IONP surface. No hysteresis is observed between the forward and backward VSM scans, indicating that both samples are superparamagnetic at room temperature.

Colloidal Stability of Pt-IONPs. Dilute aqueous Pt-IONP dispersions were evaluated by NTA (see Methods) in pure water and under similar conditions to the NP impact experiments. The particle size distribution shown in Supporting Information Figure S6 pertains to equivalent spherical diameters (ESD) as calculated from the experimentally determined range of diffusion coefficients according to the Stokes−Einstein relation. NTA results indicate that the Pt-IONPs are dispersed in pure water (pH 5−6) as relatively small aggregates with an average diffusion coefficient (D_{NP}) of 4.2 × 10^{-8} cm^2/s, which is calculated to correspond to an average ESD of 110 (±30) nm. The agglomerate of 10 Pt-IONPs shown in the STEM image of Figure 1c is a suitable representation of an aggregate of adequate size to belong within the ESD majority. We speculate that the tendency of the Pt-IONPs to aggregate is a consequence of the absence of stabilizing surfactants, which were deliberately avoided during and after synthesis to ensure that Pt surface sites remain exposed and active for catalyzing the electrooxidation of hydrazine.

All previously reported particle collisions that were detected using hydrazine oxidation as the indicator have relied on Pt or Au NPs that were originally synthesized using citrate as the capping ligand.[18,25−34] Koper and co-workers discovered that hydrazine rapidly induces aggregation of citrate-capped Pt NPs,[29] which challenges the general assumption that the majority of observed EA signals corresponds to individual Pt NP impacts. Since then, authors have noted the significance of hydrazine-induced NP aggregation to transient detection of Pt particle impacts and have applied this knowledge to designate outlying current signals of larger magnitude as EA collisions of NP aggregates.[30−34] However, the extent to which EA impact analysis becomes convoluted by colloidal instability and time dependent aggregation effects remains unassessed.

Therefore, we have begun to utilize NTA for evaluating the colloidal stability of NPs in the presence of the electrochemical indicator and electrolyte/buffer to properly correlate aggregation kinetics with particle impact collision rates. The ESD/D_{NP} distributions do not vary significantly among dispersions of Pt-IONPs prepared with pure water, sodium phosphate buffer (SPB) alone, and both SPB and N_2H_4 (Figure 6, Supporting Information Table S1). Importantly, the experimental solution conditions for EA collision analysis (15.0 mM N_2H_4 and 50.0 mM SPB) do not trigger the formation of larger aggregates of Pt-IONPs, because the particle size distributions and concentrations remain comparable to the values obtained in water. The Pt-IONP concentrations for EA collision analysis were calculated using the value of the stock Pt-IONP concentration (40 pM), which was determined by NTA of the sample prepared in a solution containing 15.0 mM N_2H_4 and 50.0 mM SPB, pH 7.5 (Supporting Information Table S1).

EA Collision Analysis of Pt-IONPs at a Au UME. Pt-IONP EA collisions were first detected using a 3-electrode setup with a 25 μm-diameter gold disk UME as the working electrode in the presence of 15.0 mM N_2H_4. To observe collision events by EA, both the NPs and electrochemical indicator must be present in solution, as schematically presented in Figure 7a. When N_2H_4 indicator is omitted, the CA scan for a suspension of 140 fM Pt-IONPs in phosphate buffer (Figure 7b, black trace) results in a flat featureless steady-state background current (with the exception of the intense noisy section at ~100 s attributed to the opening of the Faraday cage to inject a small volume of Pt-IONPs to the solution.) In the presence of N_2H_4, before adding any

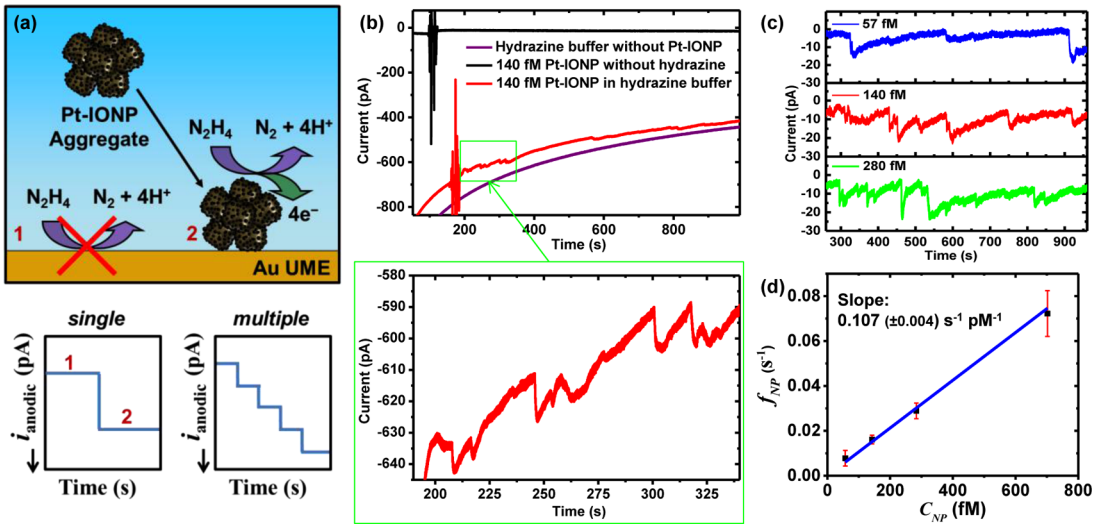

Figure 7. Chronoamperometric detection of Pt-IONP adsorption events on 25 μm diameter Au UME in the presence of 15.0 mM hydrazine, 50.0 mM sodium phosphate buffer, pH 7.5: (a) single Pt-IONP aggregate detection scheme with idealized current *vs* time response, (b) full current *vs* time trace (including overlaid control experiments in which either Pt-IONP or hydrazine indicator was not included) and zoomed in section of transient current spikes resulting from individual nanoparticle sticking events, (c) background-subtracted current *vs* time traces at three varied Pt-IONP concentrations, and (d) plot of Pt-IONP adsorption frequency, f_{NP}, (from NP collision count per 600 s) as a function of Pt-IONP concentration, C_{NP}.

Pt-IONPs to the solution, a smooth, relatively low, and decreasing background current (Figure 7b, purple trace) is observed due to the sluggish oxidation of hydrazine at a Au UME held at 0 V *vs* Ag/AgCl and Au surface fouling. As shown previously in Figure 4, the onset of N_2H_4 electrooxidation on Au UME in pH 7.5 buffer occurs at approximately 0 V *vs* Ag/AgCl.

The red CA trace was acquired for a solution containing both 15.0 mM N_2H_4 and 140 fM Pt-IONPs. Each small sharp increase in anodic current marks the steady-state electrocatalytic oxidation of hydrazine at a Pt-IONP aggregate that has made electrical contact with the Au UME. The CA signals are primarily sawtooth shaped with a quick, sharp increase in the anodic current followed by a slower rate of decrease. The continuously decaying background current appears to be largely accountable for the difference in the EA signal shape from the ideal staircase response (Figure 7a), but the slow deactivation of the adsorbed Pt-IONPs over time is also likely to contribute. This deactivation effect has also been noted previously for hydrazine-induced EA sticking collisions of citrate-capped Pt NPs on Au or carbon fiber UMEs.[33] The background-subtracted CA traces in Figure 7c more appropriately represent the EA collision responses and the relatively slow rates of adsorbed Pt-IONP deactivation.

The effect of Pt-IONP concentration on the frequency of particle/electrode collision events is also presented in Figure 7c. As shown in Figure 7d, a clear linear trend relates the observed EA collision frequency, f_{NP}, of Pt-IONP aggregates to their respective bulk concentration, C_{NP}. The slope of the calibration curve is 0.107 ($\pm$0.004) s^{-1} pM^{-1}, which is the experimentally derived Pt-IONP collision rate (R_{coll}). The theoretical prediction of R_{coll} was calculated to be 0.13 ($\pm$0.06) s^{-1} pM^{-1} according to the steady-state diffusive flux of Pt-IONP aggregates to a disk UME,

$$R_{coll} = f_{NP}C_{NP}^{-1} = 4N_A D_{NP} r \quad (1)$$

where N_A is Avogadro's number, r is the radius of the disk UME, and D_{NP} is the Pt-IONP diffusion coefficient acquired from NTA, $(4 \pm 2) \times 10^{-8}$ cm^2/s (Supporting Information Table S1). The experimentally determined D_{NP} was calculated to be $(3.5 \pm 0.1) \times 10^{-8}$ cm^2/s, fitting well within the broad range of D_{NP} values resulting from NTA. The standard error associated with the EA collision curve is far lower than that reported by NTA. We are careful not to misinterpret this result as representing the relative analytical precision between the two methods. The broad range of diffusion coefficients resulted from NTA is a more statistically meaningful representation the Pt-IONP aggregate D_{NP} distribution because the tracking analysis pools from a much larger sample population: ~1000 NP tracks per analysis. This contrasts with the total number of NP impacts counted for a single 600 s CA analysis time, which ranged from 3 to 50 counts for 57 to 700 fM Pt-IONP concentrations, respectively. The error bars are especially small for the lower NP concentrations, because only a very small number of particles can be detected in the allotted time, thus the variability between 3 replicate CA scans is relatively low compared to measurements at higher concentrations (Figure 7c).

As mentioned earlier, the experimental collision rate matches well with the calculated prediction according to eq 1, which assumes that NP adsorption is not kinetically

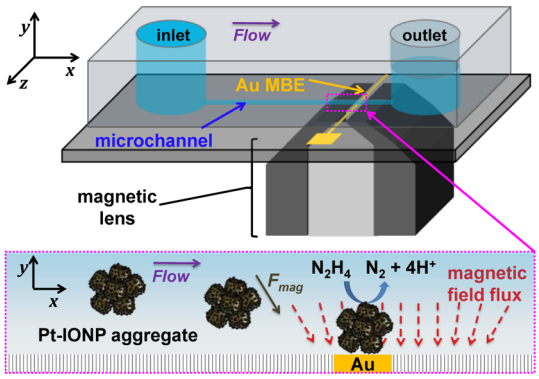

Scheme 2. Schematic of microfluidic device with attached magnetic lens.

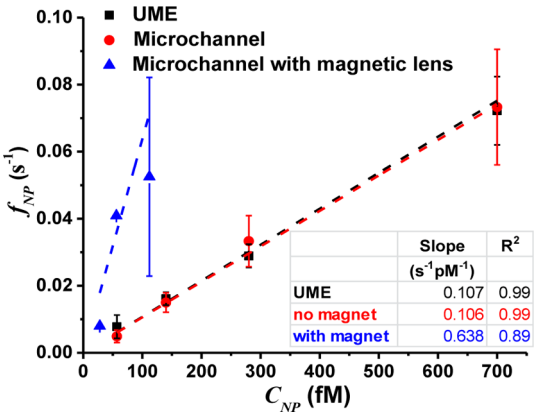

Figure 8. Summary of Pt-IONP collision frequency analysis: nanoparticle collision frequency with respect to concentration for UME and microfluidic experiments with and without magnetic lens applied. Embedded table lists corresponding slopes (collision rates) and R^2 coefficients.

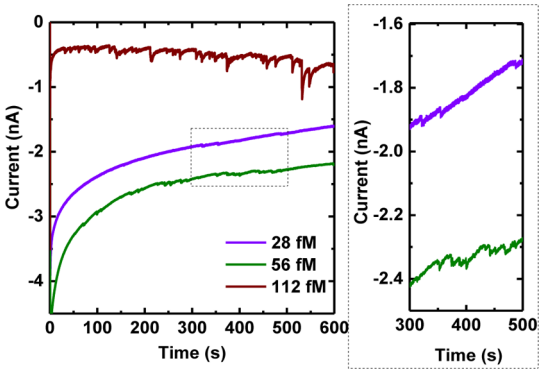

Figure 9. Chronoamperometric detection of magnetic field driven Pt-IONP adsorption events on 25 μm × 25 μm Au MBE in microfluidic device with attached magnetic lens in the presence of 15.0 mM hydrazine, 50.0 mM sodium phosphate buffer, pH 7.5.

hindered at the electrode/solution interface. This result is contrary to what has been reported previously for citrate-capped Pt NP collision experiments performed under comparable conditions, in which the experimentally determined collision rates were found to be at least 1 order of magnitude lower than expected for diffusive transport.[25,27,30] We must note that unlike these earlier studies our NP concentrations are accurately measured using NTA, and as discussed earlier, the NPs are stable (*i.e.*, do not undergo hydrazine-induced NP aggregation) on the time scale of the analysis.[29]

EA Collision Analysis of Pt-IONPs in Microfluidic Device. A schematic of the microfluidic device is shown in Scheme 2. Pt-IONPs are transported along the microchannel by pressure-driven flow. A gold microband electrode (MBE) is positioned at the bottom of the channel, its long axis configured perpendicular to the direction of flow. Collision experiments were performed in the microfluidic device using the same NP concentrations and solution conditions as those used for NP collisions at the Au UME disk discussed earlier. As shown in Supporting Information Figure S7, no signals are observed in the absence of Pt-IONPs. The overall size and shape of the EA collision current responses are comparable to those observed at the Au UME. Pt-IONP collision frequencies are also comparable (Figure 8). Because the Au UME and MBE are of similar dimensions, this result suggests that the pressure-driven flow does not make a substantial convective contribution to the Pt-IONP mass transport vector along the *y* direction (Scheme 2).

Influence of Applied Magnetic Field. A "magnetic lens" was constructed by adopting the design of Wheeler and co-workers.[71] As shown in Scheme 2 and Supporting Information Figure S8, the magnetic lens is positioned below the microfluidic device so that the magnetic field is concentrated at the Au MBE. The ability of the magnetic lens to attract the Pt-IONPs was assessed by optical microscopy of a relatively high concentration (44 pM) of Pt-IONPs flowing through a microfluidic device (Supporting Information Figure S9). The magnetic lens was found to be effective toward attracting and accumulating Pt-IONPs to a small area at the bottom of the channel. This experiment also provided visual guidance for proper alignment of the magnetic lens with the Au MBE.

EA collision experiments were next performed in the microfluidic device with the magnetic lens in place. The resulting current transients are presented in Figure 9 at varied concentrations and the corresponding plot of collision frequency with respect to Pt-IONP concentration is shown in Figure 8. At Pt-IONP concentrations below 60 fM, the size of the EA collision event signals are comparable to those observed without the application of a magnetic field (5−50 pA range), while substantially larger CA collision signals (>150 pA) are observed at the highest concentration (112 fM). We attribute these bigger collision events to larger aggregates at higher concentrations, because larger aggregates are assumed to produce collision signals with relatively greater current magnitude due to the overall increase in Pt surface area per aggregate. The formation of larger aggregates is likely accelerated

by interparticle attractive forces due to the influence of the magnetic field (not accounted for in the NTA measurements). Magnetic field-induced agglomeration has also been reported by Compton and coworkers[37] while investigating the "cathodic particle coulometry" of ~24 nm-diameter uncapped Fe_3O_4 nanoparticles at similar concentrations (10^{-8} g mL^{-1} or 100−1000 fM) as the Pt-IONP sample herein discussed (112 fM). As shown in Figure S10 of Supporting Information, the average current magnitude of EA collision transients resulting after application of the magnetic field is enhanced by about a factor of 5 in comparison to the collision events recorded in the microfluidic cell without magnetization of the Pt-IONPs, indicative of magnetically induced aggregation. The average calculated Pt ECSA based on surface specific activity (350 mA/cm^2 in 15.0 mM N_2H_4) is presented in Supporting Information Figure S10b. Without the magnetic lens in place, the average Pt ECSA per suspended Pt-IONP aggregate is roughly 0.001 μm^2, whereas the average Pt ECSA from the EA collision events of Pt-IONPs under the influence of the applied magnetic field was estimated to be about 0.006 μm^2.

Another complication at higher Pt-IONP concentrations is surface saturation of the Au MBE with Pt-IONPs. This results in a depletion of the available surface area for subsequent collisions, thereby significantly decreasing the frequency of collision events at longer times. Accordingly, we suspect that both the effect of magnetically induced aggregation and electrode saturation collectively contribute to the relatively large range of error associated with the 112 fM sample concentration. For the very low level biosensing applications we have in mind for this approach, this is not a serious problem. Although the relationship between collision frequency and concentration is not highly linear (R^2 = 0.89) (possibly also due to the aforementioned phenomena), the collision rate was estimated as ~0.64 s^{-1} pM^{-1} from the correlation in Figure 8. Upon comparison to the collision rate without any applied magnetic field (0.11 s^{-1} pM^{-1}), we infer that the rate is enhanced approximately 6-fold due to the application of the magnetic lens.

CONCLUSIONS

A stepwise synthetic method was developed to achieve hybrid Pt-decorated iron oxide nanoparticles that are dispersible as colloidally stable aggregates in dilute aqueous suspensions. The mechanism of adsorption of Pt^{2+} complex precursors onto IONP substrates and subsequent transformation to Pt-IONPs was investigated by a combination of spectroscopic and microscopic methods, thus revealing the necessary roles of hydroxylamine and dopamine toward the formation of a uniform coating of Pt^{2+} on the Pt^{2+}-IONP intermediate structure. The hybrid NPs exhibit the intended dual electrocatalytic and superparamagnetic properties. NTA was utilized to appropriately characterize colloidal stability and quantify NP suspensions for EA collision analysis. Individual impacts of Pt-IONPs on the Au UME were detected *via* electrocatalytic amplification in the presence of hydrazine. The Pt-IONP collision frequency followed a linear dependence with concentration and correlated well with theory, which is unprecedented for an EA-based collision system. The collision rate of Pt-IONPs on the Au MBE in a microfluidic electrochemical cell was found to match that of the Au UME experiments. The relative frequency of Pt-IONP impact events increased 6-fold upon the application of a tightly focused magnetic field to the Au MBE, establishing proof-of-concept that bifunctional magnetic/catalytic nanoparticles can be utilized for enhancing mass transport to the working electrode.

Future optimizations will focus more on the microfluidic device than the bifunctional NPs in order to achieve a higher collision rate and lower LOD. The major issue with the present configuration is that the magnetic field is focused to a width of ~500 μm while the width of the microelectrode is only 25 μm, which suggests that only about 5% of the Pt-IONPs captured by the magnetic lens actually interact with the Au MBE and generate a current signal. We are currently investigating strategies for negotiating a better match between the applied magnetic field flux density profile and the working electrode with the expectation of significantly improving Pt-IONP capturing efficiency. After an optimized integrated microfluidic magnetic device is established using the Pt-IONPs as probes, our next goal is to adopt NP biomodification strategies in order to transform this unique NP sensing methodology into a general platform for the detection of biomolecule targets of interest at ultratrace concentrations.

METHODS

Chemicals. Potassium tetrachloroplatinate (K_2PtCl_4, 99.9%), iron(III) chloride hexahydrate ($FeCl_3 \cdot 6H_2O$, 97%), 3-hydroxytyramine hydrochloride (dopamine, ACS grade), Nafion solution (5% wt in lower aliphatic alcohols/H_2O mix), and chloroform were obtained from Sigma-Aldrich. Hydroxylamine hydrochloride ($NH_2OH \cdot HCl$, ACS grade), sodium borohydride ($NaBH_4$, 98%), sodium oleate (purified), sodium phosphate monobasic monohydrate (ACS grade), sodium phosphate dibasic anhydrous (ACS grade), sulfuric acid (H_2SO_4, ACS grade), nitric acid (HNO_3, ACS grade), hydrochloric acid (HCl, ACS grade), and acetone (ACS grade) were purchased from Fisher Scientific. Absolute ethanol (ACS grade) was obtained from Pharmco-Aaper. Hydrazine sulfate (ACS grade), nitrosonium tetrafluoroborate ($NOBF_4$, 97%), and oleic acid (97%) were purchased from Acros Organics. Carbon black (Vulcan XC72, VC) was obtained from Cabot Corp. All water was

purified to 18.2 MΩ·cm using a Barnstead Epure System. All chemicals were used as received.

Synthesis of OA-IONPs. All synthesis glassware was washed with *aqua regia*, neutralized, rinsed thoroughly, and dried before use. Iron−oleate complex was synthesized according to the method reported by Park *et al.*[72] For a typical synthesis of $Fe_{1-x}O/Fe_3O_4$ core/shell nanocubes, iron oleate complex (1.8 g, 2 mmol) and oleic acid (212 μL, 1 mmol) were dissolved in 13 mL of 1-octadecene in a 50 mL 3-necked flask by heating to 80 °C. The mixture was then degassed by alternating vacuum and N_2 purging by standard Schlenk line technique. The reaction mixture was then heated without stirring at a rate of 4−5 °C/min by applying 70 W power to a heating mantle. When the temperature of the mixture reached 240 °C, the power was increased to 80 W so that the temperature increased a rate of 2−3 °C/min. The reaction was left to react at 300−305 °C for 1 h before the heating mantle was turned off. After cooling to room temperature, 40 mL of hexanes was added to suspend product, followed by 15 mL of ethanol to cause the $Fe_{1-x}O/Fe_3O_4$ nanocubes to precipitate out of suspension. The product was collected by centrifugation and purified by suspending in hexanes and precipitating again with ethanol. This process was repeated two more times to remove impurities.

Removal of Oleate Ligands from OA-IONPs. The procedure reported by Dong *et al.* was followed for ligand removal and phase transfer of the iron oxide nanoparticles, with some modifications.[48] For a typical reaction, 40 mg of OA-IONPs was suspended in a mixture of 8 mL of hexanes and 40 μL of oleic acid followed by precipitation upon the addition of 4 mL of ethanol. The precipitate was collected by an external magnet and then resuspended in 8 mL of hexanes. $NOBF_4$ (20 mg) was sonicated in 8 mL of chloroform for about 30 s. The resulting saturated solution was added to the OA-IONP/hexanes suspension and sonicated for 15 s. The resulting precipitate was collected by magnet and redispersed in 4 mL of DMF. Toluene was then added to precipitate the iron oxide nanocubes. After two more rinses with toluene to remove organic impurities, the IONPs were washed three times with a solvent mixture of 25% water and 75% ethanol to remove excess salts.

Dopamine Modification To Prepare AT-IONPs. Immediately following the last rinsing step above, the resulting wet IONP sample (~40 mg, assuming complete magnetic recovery) was suspended in a solution containing dopamine (32 mg) in 20 mL of water and 8 mL of ethanol. The reaction mixture was agitated in a sonication bath for 3 h at room temperature. The resulting AT-IONPs were collected with a magnet and rinsed three times with ethanol, dried at room temperature under a gentle stream of nitrogen, then redispersed in distilled water.

Synthesis of Pt^{2+}-IONPs. AT-IONP (10 mg) was mixed with 70 mL of water in a 250 mL round-bottom flask. The mixture was agitated into suspension by sonication for 15 min in a 60 °C sonication bath. A 20 mL aqueous solution containing 30 mg of K_2PtCl_4 was then added. After 30 min of sonication, a solution of $NH_2OH·HCl$ (70 mg) in 10 mL of 50 mM sodium phosphate buffer (pH 7.5) was added. After 2 h reacting under constant sonication at 60 °C, the Pt^{2+}-IONP product was isolated by centrifugation and rinsing once with 0.010 M NaOH followed by three washings with water, using a permanent magnet to collect Pt^{2+}-IONPs between rinses. A series of control syntheses were carried out using the same procedure as described above except using (a) naked IONPs without adding $NH_2OH·HCl$, (b) naked IONPs with NH_2OH, (c) AT-IONPs without NH_2OH, and (d) AT-IONPs with NH_2OH.

Synthesis of Pt-IONPs. A 10 mg portion of Pt^{2+}-IONPs was sonicated in 90 mL of water for 10 min. A solution containing $NaBH_4$ (40 mg) in 10 mL of water was then added, and the mixture was sonicated for 2 h at room temperature. Pt-IONP product was magnetically isolated and washed with water 3 times.

Nanoparticle Characterization. Scanning transmission electron microscopy (STEM) and energy dispersive X-ray spectroscopy (EDX) were performed using a Hitachi-S5500 microscope operated at 30 kV equipped with a Bruker Quantax 4010 EDX detector. High-resolution imaging was carried out with a JEOL 2010F transmission electron microscope (TEM). Samples were prepared for electron microscopy by dropping nanoparticle suspensions onto Formvar-coated copper TEM grids (FCF400-Cu, Electron Microscopy Sciences) and drying at 50 °C. Powder X-ray diffraction (XRD) was performed on a Rigaku R-axis Spider diffractometer using Cu Kα radiation. X-ray photoelectron spectroscopy (XPS) was performed on a Kratos AXIS Ultra DLD spectrometer equipped with a monochromatic Al X-ray source (Al α, 1.4866 keV). All spectral peak positions were calibrated to adventitious carbon C 1s at 284.5 eV, and peak areas were calculated using CasaXPS software with a standard Gaussian/Lorentzian fit and Shirley background. Magnetometry measurements were acquired using aqueous concentrated 0.5% (v/v) AT-IONP and Pt-IONP samples at room temperature with a vibrating sample magnetometer (VSM, Lake Shore 7307). Nanoparticle tracking analysis (NTA) was performed using a NanoSight NS500 Instrument operating in scatter mode using a 638 nm laser at 40 mW power. Samples were diluted 100-fold from their 40 pM stock suspension and allowed to sit for at least 1 h before analysis. A total of 10 1-min video acquisitions were taken for each sample, automatically flowing a different portion of the sample into the detection volume in between each measurement. The plots in Figure 6 were produced after averaging all ten NTA acquisitions per sample.

Electrochemical Methods. All nonmicrofluidic electrochemical measurements (cyclic voltammetry and chronoamperometry) were performed using a CH700 potentiostat from CH instruments. Unless otherwise noted, a gold wire and Ag/AgCl (sat. KCl, CH Instruments) electrodes were used as the counter and reference electrodes, respectively. For the voltammetric electrocatalytic evaluation of Pt-IONPs for hydrazine oxidation, catalyst films on rotating disk glassy carbon electrodes (3 mm diameter, Metrohm) were used as the working electrodes. All VC-supported catalyst inks were prepared by sonicating 20 wt % Pt NP with 80 wt % VC in 0.05 wt % Nafion in 1/1 (v/v) ethanol−water for 30 min to make a total 1 mg/mL catalyst ink, from which a 6 μL aliquot was drop-casted onto a polished glassy carbon electrode (3 mm diameter) in 2 μL intervals while drying under rotation at 700 rpm to result in a thin uniform film containing 6 μg of catalyst. Pt electroactive surface area (ECSA) measurements were performed on the Pt-IONP catalyst film by first recording a CV at 20 mV/s scan rate in N_2-purged 0.10 M KOH to obtain the background current associated with Fe^{2+}/Fe^{3+} redox couple. Next, the electrolyte solution was bubbled with CO gas for 650 s while holding the electrode potential at −0.6 V *vs* $Hg/HgSO_4$. After the solution was purged with N_2 gas for 30 m, a second CV was acquired. The anodic scan of the former CV was subtracted from the latter to isolate the CO stripping peak. The background-corrected CO stripping peak was integrated with respect to time to determine the charge (6.14 μC) used to estimate Pt ECSA on the catalyst film. The kinetic current contribution (i_K) from electrocatalytic hydrazine oxidation on the Pt-IONP catalyst film held at 0 V *vs* Ag/AgCl was determined from the intercept of the Koutecky−Levich plot[73] shown in Supporting Information Figure S5b. The Pt surface specific electrocatalytic activity (34.9 mA/cm^2) was calculated by dividing i_K (0.509 mA) by the Pt ECSA value (0.0146 cm^2).

Chronoamperometric Pt-IONP collision experiments were first performed using a Au UME as the working electrode. The Au UME was fabricated by sealing a Au microwire (25 μm diameter) in melted glass capillary. Au UME was polished with 0.05 μm Al_2O_3 powder, sonicated in 1:1 ethanol/water mixture, then cycled in 0.1 M H_2SO_4 from −0.8 to 1.15 V *vs* $Hg/HgSO_4$ (sat. K_2SO_4, CH instruments) at 0.4 V/s until Au oxide peaks were consistent (about 50 cycles). A 14 mL aliquot of 15 mM N_2H_4 in 50 mM SPB (pH 7.5) was first introduced to a 20 mL vial and bubbled with argon. After about 80 s of CA acquisition, an aliquot (ranging from 20 to 250 μL) of the Pt-IONP stock suspension (40 pM) was injected *via* pipet into the vial. To ensure proper distribution of Pt-IONPs in solution, the solution was bubbled with argon for 10 s after injecting NPs. The electrochemical cell (20 mL glass vial) was housed within a Faraday cage (CH instruments). Current was recorded at constant potential of 0 V *vs* Ag/AgCl throughout the 1000 s analysis time. Collision events were counted in the time range between 300 and 900 s for frequency analysis.

For the microfluidic electrochemical cell, standard photolithographic method was used to fabricate both the channel and the gold microband electrode (Au MBE).[74] The channel dimension is 10 mm (l) × 25 μm (w) × 19 μm (h) and a 4 mm (d) punch was used to punch out both the inlet and the outlet. The base of the fluidic channel consisted of a glass slide, onto which a 25 μm (w) Au MBE had been microfabricated. The polydimethylsiloxane (PDMS) monolith and glass base were then bound together. After annealing the PDMS and the Au electrode, 60 and 20 μL of 100 mM phosphate buffer (pH 7.4) were injected into the inlet and the outlet. A small Ag/AgCl leakless reference electrode (3.4 M KCl filling solution, model 66-EE0009, Dionex, Bannockburn, IL) was placed in the outlet reservoir and used as both the reference and counter electrodes in a two-electrode configuration. Electrochemical measurements were performed on the microfluidic device housed within a Faraday cage constructed from copper plate and mesh. CV and CA scans were recorded using a Chem-Clamp voltammeter-amperometer (Dagan Corp.) and a PAR 175 Universal Function Generator from Princeton Applied Research. The acquired data was translated using a custom program written in LabView 2010 (National Instruments). The Au microband electrode was cleaned by scanning from −0.2 to 1.2 V *vs* Ag/AgCl at 100 mV/s until the scans equilibriated. Afterward, solutions in both reservoirs were removed and replaced with hydrazine solution (15 mM N_2H_4, 50 mM phosphate, pH 7.4) that was purged with nitrogen in advance. To record the background cyclic voltammogram, the potential was swept from −0.2 to 0.2 V *vs* Ag/AgCl at 20 mV/s. For the background it-curve, the potential was held at 0 V *vs* Ag/AgCl for 600 s with the sampling interval of 15 ms. For collision experiments without the magnet, appropriate amount of Pt-IONPs were injected into the hydrazine solution and vortexed. The solution in the inlet was replaced with the same volume of the hydrazine solution with the NPs and current was recorded over 600 s time period. For the collision experiments with the magnet, the device was taped down on the magnetic platform so that the middle of the magnetic lens is positioned 450 μm downstream of the Au MBE. The Pt-IONP suspension in hydrazine with buffer was injected followed by recording current over a 600 s time period. The magnetic lens was fabricated following the procedure reported by Wheeler and co-workers.[71]

Conflict of Interest: The authors declare no competing financial interest.

Supporting Information Available: TEM time-lapse video (12× rate increase) of electron beam-induced Pt^0 nucleation and growth, powder XRD characterization, STEM/EDX analysis of synthetic mechanism, XP spectra/quantitative analysis, supplemental NTA results, CA in microfluidic channel, photographs of microfluidic device, and microscopic assessment of Pt-IONP magnetic capture in microfluidic channel. The Supporting Information is available free of charge on the ACS Publications website at DOI: 10.1021/acsnano.5b02892.

Acknowledgment. We thank the Defense Threat Reduction Agency (DTRA) (grant HDTRA1-11-1-0005) for financial support and the Welch Summer Scholars Program (Grant H-F-0001) at UT-Austin. K.J.S. acknowledges the Robert A. Welch Foundation for support (Grant F-1529). R.M.C. thanks the Robert A. Welch Foundation (Grant F-0032) for sustained research support. D.A.R. gratefully acknowledges A. T. Fischer (Abbott Diagnostics) and A. R. Wheeler (Univ. of Toronto) for assisting with magnetic lens assembly, N. Membreno (UT-Austin) for TEM acquisition, M. R. Charlton (UT-Austin) for XPS acquisition, and S. Kong (UT-Austin) for VSM. We also thank A. J. Bard (UT-Austin), B. Zhang (Univ. of Washington), and R. E. Schaak (Penn State) for insightful discussions.

REFERENCES AND NOTES

1. Costi, R.; Saunders, A. E.; Banin, U. Colloidal Hybrid Nanostructures: A New Type of Functional Materials. *Angew. Chem., Int. Ed.* **2010**, *49*, 4878–4897.
2. Bard, A. J.; Zhou, H.; Kwon, S. J. Electrochemistry of Single Nanoparticles *via* Electrocatalytic Amplification. *Isr. J. Chem.* **2010**, *50*, 267–276.
3. Van Reenen, A.; de Jong, A. M.; den Toonder, J. M. J.; Prins, M. W. J. Integrated Lab-on-Chip Biosensing Systems Based on Magnetic Particle Actuation − a Comprehensive Review. *Lab Chip* **2014**, *14*, 1966.
4. Pankhurst, Q. A.; Thanh, N. K. T.; Jones, S. K.; Dobson, J. Progress in Applications of Magnetic Nanoparticles in Biomedicine. *J. Phys. D: Appl. Phys.* **2009**, *42*, 224001/1–224001/15.
5. Reddy, L. H.; Arias, J. L.; Nicolas, J.; Couvreur, P. Magnetic Nanoparticles: Design and Characterization, Toxicity and Biocompatibility, Pharmaceutical and Biomedical Applications. *Chem. Rev.* **2012**, *112*, 5818–5878.
6. Yoo, D.; Lee, J.-H.; Shin, T.-H.; Cheon, J. Theranostic Magnetic Nanoparticles. *Acc. Chem. Res.* **2011**, *44*, 863–874.
7. Latham, A. H.; Williams, M. E. Controlling Transport and Chemical Functionality of Magnetic Nanoparticles. *Acc. Chem. Res.* **2008**, *41*, 411–420.
8. Beveridge, J. S.; Stephens, J. R.; Williams, M. E. The Use of Magnetic Nanoparticles in Analytical Chemistry. *Annu. Rev. Anal. Chem.* **2011**, *4*, 251–273.
9. Lim, J.; Lanni, C.; Evarts, E. R.; Lanni, F.; Tilton, R. D.; Majetich, S. A. Magnetophoresis of Nanoparticles. *ACS Nano* **2011**, *5*, 217–226.
10. Yan, H.; Wu, H. Magnetophoresis. In *Encyclopedia of Microfluidics and Nanofluidics*; Li, D., Ed.; Springer: New York, NY, 2014; pp 1−8.
11. Gijs, M. A. M.; Lacharme, F.; Lehmann, U. Microfluidic Applications of Magnetic Particles for Biological Analysis and Catalysis. *Chem. Rev.* **2010**, *110*, 1518–1563.
12. Peng, Z.; Yang, H. Designer Platinum Nanoparticles: Control of Shape, Composition in Alloy, Nanostructure and Electrocatalytic Property. *Nano Today* **2009**, *4*, 143–164.
13. Ding, L.; Bond, A. M.; Zhai, J.; Zhang, J. Utilization of Nanoparticle Labels for Signal Amplification in Ultrasensitive Electrochemical Affinity Biosensors: A Review. *Anal. Chim. Acta* **2013**, *797*, 1–12.
14. Zhu, N.; Chang, Z.; He, P.; Fang, Y. Electrochemical DNA Biosensors Based on Platinum Nanoparticles Combined Carbon Nanotubes. *Anal. Chim. Acta* **2005**, *545*, 21–26.
15. Polsky, R.; Gill, R.; Kaganovsky, L.; Willner, I. Nucleic Acid-Functionalized Pt Nanoparticles: Catalytic Labels for the Amplified Electrochemical Detection of Biomolecules. *Anal. Chem.* **2006**, *78*, 2268–2271.
16. Spain, E.; Brennan, E.; McArdle, H.; Keyes, T. E.; Forster, R. J. High Sensitivity DNA Detection Based on Regioselectively Decorated Electrocatalytic Nanoparticles. *Anal. Chem.* **2012**, *84*, 6471–6476.
17. Kwon, S. J.; Bard, A. J. DNA Analysis by Application of Pt Nanoparticle Electrochemical Amplification with Single Label Response. *J. Am. Chem. Soc.* **2012**, *134*, 10777–10779.
18. Alligrant, T. M.; Nettleton, E. G.; Crooks, R. M. Electrochemical Detection of Individual DNA Hybridization Events. *Lab Chip* **2013**, *13*, 349–354.
19. Spain, E.; Brennan, E.; Keyes, T. E.; Forster, R. J. Dual Function Metal Nanoparticles: Electrocatalysis and DNA Capture. *Electrochim. Acta* **2014**, *128*, 61–66.
20. Rees, N. V.; Zhou, Y.-G.; Compton, R. G. Making Contact: Charge Transfer during Particle−electrode Collisions. *RSC Adv.* **2012**, *2*, 379.
21. Rees, N. V. Electrochemical Insight from Nanoparticle Collisions with Electrodes: A Mini-Review. *Electrochem. Commun.* **2014**, *43*, 83–86.
22. Cheng, W.; Compton, R. G. Electrochemical Detection of Nanoparticles by "nano-Impact" Methods. *TrAC, Trends Anal. Chem.* **2014**, *58*, 79–89.
23. Kleijn, S. E. F.; Lai, S. C. S.; Koper, M. T. M.; Unwin, P. R. Electrochemistry of Nanoparticles. *Angew. Chem., Int. Ed.* **2014**, *53*, 3558–3586.
24. Xiao, X.; Bard, A. J. Observing Single Nanoparticle Collisions at an Ultramicroelectrode by Electrocatalytic Amplification. *J. Am. Chem. Soc.* **2007**, *129*, 9610–9612.

25. Xiao, X.; Fan, F.-R. F.; Zhou, J.; Bard, A. J. Current Transients in Single Nanoparticle Collision Events. *J. Am. Chem. Soc.* **2008**, *130*, 16669–16677.
26. Xiao, X.; Pan, S.; Jang, J. S.; Fan, F.-R. F.; Bard, A. J. Single Nanoparticle Electrocatalysis: Effect of Monolayers on Particle and Electrode on Electron Transfer. *J. Phys. Chem. C* **2009**, *113*, 14978–14982.
27. Kwon, S. J.; Zhou, H.; Fan, F.-R. F.; Vorobyev, V.; Zhang, B.; Bard, A. J. Stochastic Electrochemistry with Electrocatalytic Nanoparticles at Inert Ultramicroelectrodes-Theory and Experiments. *Phys. Chem. Chem. Phys.* **2011**, *13*, 5394–5402.
28. Zhou, H.; Park, J. H.; Fan, F.-R. F.; Bard, A. J. Observation of Single Metal Nanoparticle Collisions by Open Circuit (Mixed) Potential Changes at an Ultramicroelectrode. *J. Am. Chem. Soc.* **2012**, *134*, 13212.
29. Kleijn, S. E. F.; Serrano-Bou, B.; Yanson, A. I.; Koper, M. T. M. Influence of Hydrazine-Induced Aggregation on the Electrochemical Detection of Platinum Nanoparticles. *Langmuir* **2013**, *29*, 2054–2064.
30. Dasari, R.; Robinson, D. A.; Stevenson, K. J. Ultrasensitive Electroanalytical Tool for Detecting, Sizing, and Evaluating the Catalytic Activity of Platinum Nanoparticles. *J. Am. Chem. Soc.* **2013**, *135*, 570–573.
31. Dasari, R.; Walther, B.; Robinson, D. A.; Stevenson, K. J. Influence of the Redox Indicator Reaction on Single-Nanoparticle Collisions at Mercury- and Bismuth-Modified Pt Ultramicroelectrodes. *Langmuir* **2013**, *29*, 15100–15106.
32. Dasari, R.; Tai, K.; Robinson, D. A.; Stevenson, K. J. Electrochemical Monitoring of Single Nanoparticle Collisions at Mercury-Modified Platinum Ultramicroelectrodes. *ACS Nano* **2014**, *8*, 4539–4546.
33. Guo, Z.; Percival, S. J.; Zhang, B. Chemically Resolved Transient Collision Events of Single Electrocatalytic Nanoparticles. *J. Am. Chem. Soc.* **2014**, *136*, 8879–8882.
34. Alligrant, T. M.; Anderson, M. J.; Dasari, R.; Stevenson, K. J.; Crooks, R. M. Single Nanoparticle Collisions at Microfluidic Microband Electrodes: The Effect of Electrode Material and Mass Transfer. *Langmuir* **2014**, *30*, 13462–13469.
35. Castañeda, A. D.; Alligrant, T. M.; Loussaert, J. A.; Crooks, R. M. Electrocatalytic Amplification of Nanoparticle Collisions at Electrodes Modified with Polyelectrolyte Multilayer Films. *Langmuir* **2015**, *31*, 876–885.
36. Tschulik, K.; Haddou, B.; Omanović, D.; Rees, N. V.; Compton, R. G. Coulometric Sizing of Nanoparticles: Cathodic and Anodic Impact Experiments Open Two Independent Routes to Electrochemical Sizing of Fe_3O_4 Nanoparticles. *Nano Res.* **2013**, *6*, 836–841.
37. Tschulik, K.; Compton, R. G. Nanoparticle Impacts Reveal Magnetic Field Induced Agglomeration and Reduced Dissolution Rates. *Phys. Chem. Chem. Phys.* **2014**, *16*, 13909.
38. Santos, G. P.; Melo, A. F. A. A.; Crespilho, F. N. Magnetically Controlled Single-Nanoparticle Detection *via* Particle-Electrode Collisions. *Phys. Chem. Chem. Phys.* **2014**, *16*, 8012–8018.
39. Yoo, J. J.; Anderson, M. J.; Alligrant, T. M.; Crooks, R. M. Electrochemical Detection of Insulating Beads at Subattomolar Concentration *via* Magnetic Enrichment in a Microfluidic Device. *Anal. Chem.* **2014**, *86*, 4302–4307.
40. Hai, H. T.; Yang, H. T.; Kura, H.; Hasegawa, D.; Ogata, Y.; Takahashi, M.; Ogawa, T. Size Control and Characterization of Wustite (core)/spinel (shell) Nanocubes Obtained by Decomposition of Iron Oleate Complex. *J. Colloid Interface Sci.* **2010**, *346*, 37–42.
41. Gražulis, S.; Chateigner, D.; Downs, R. T.; Yokochi, A. F. T.; Quirós, M.; Lutterotti, L.; Manakova, E.; Butkus, J.; Moeck, P.; Le Bail, A. Crystallography Open Database – an Open-Access Collection of Crystal Structures. *J. Appl. Crystallogr.* **2009**, *42*, 726–729.
42. Hou, Y.; Xu, Z.; Sun, S. Controlled Synthesis and Chemical Conversions of FeO Nanoparticles. *Angew. Chem., Int. Ed.* **2007**, *46*, 6329–6332.
43. Sun, X.; Frey Huls, N.; Sigdel, A.; Sun, S. Tuning Exchange Bias in Core/Shell FeO/Fe_3O_4 Nanoparticles. *Nano Lett.* **2012**, *12*, 246–251.
44. Chalasani, R.; Vasudevan, S. Form, Content, and Magnetism in Iron Oxide Nanocrystals. *J. Phys. Chem. C* **2011**, *115*, 18088–18093.
45. Pichon, B. P.; Gerber, O.; Lefevre, C.; Florea, I.; Fleutot, S.; Baaziz, W.; Pauly, M.; Ohlmann, M.; Ulhaq, C.; Ersen, O.; et al. Microstructural and Magnetic Investigations of Wüstite-Spinel Core-Shell Cubic-Shaped Nanoparticles. *Chem. Mater.* **2011**, *23*, 2886–2900.
46. Khurshid, H.; Li, W.; Chandra, S.; Phan, M.-H.; Hadjipanayis, G. C.; Mukherjee, P.; Srikanth, H. Mechanism and Controlled Growth of Shape and Size Variant Core/shell FeO/Fe_3O_4 Nanoparticles. *Nanoscale* **2013**, *5*, 7942–7952.
47. Wetterskog, E.; Tai, C.-W.; Grins, J.; Bergström, L.; Salazar-Alvarez, G. Anomalous Magnetic Properties of Nanoparticles Arising from Defect Structures: Topotaxial Oxidation of $Fe_{1-x}O|Fe_{3-\delta}O_4$ Core|Shell Nanocubes to Single-Phase Particles. *ACS Nano* **2013**, *7*, 7132–7144.
48. Dong, A.; Ye, X.; Chen, J.; Kang, Y.; Gordon, T.; Kikkawa, J. M.; Murray, C. B. A Generalized Ligand-Exchange Strategy Enabling Sequential Surface Functionalization of Colloidal Nanocrystals. *J. Am. Chem. Soc.* **2011**, *133*, 998–1006.
49. Yuen, A. K. L.; Hutton, G. A.; Masters, A. F.; Maschmeyer, T. The Interplay of Catechol Ligands with Nanoparticulate Iron Oxides. *Dalton Trans.* **2012**, *41*, 2545–2559.
50. Mazur, M.; Barras, A.; Kuncser, V.; Galatanu, A.; Zaitzev, V.; Turcheniuk, K. V.; Woisel, P.; Lyskawa, J.; Laure, W.; Siriwardena, A.; et al. Iron Oxide Magnetic Nanoparticles with Versatile Surface Functions Based on Dopamine Anchors. *Nanoscale* **2013**, *5*, 2692–2702.
51. Robinson, D. A.; Stevenson, K. J. Uniform Epitaxial Growth of Pt on Fe_3O_4 Nanoparticles; Synergetic Enhancement to Pt Activity for the Oxygen Reduction Reaction. *J. Mater. Chem. A* **2013**, *1*, 13443–13453.
52. Turkevich, J.; Stevenson, P. C.; Hillier, J. A Study of the Nucleation and Growth Processes in the Synthesis of Colloidal Gold. *Discuss. Faraday Soc.* **1951**, *11*, 55–75.
53. Brown, K. R.; Natan, M. J. Hydroxylamine Seeding of Colloidal Au Nanoparticles in Solution and on Surfaces. *Langmuir* **1998**, *14*, 726–728.
54. Lyon, J. L.; Fleming, D. A.; Stone, M. B.; Schiffer, P.; Williams, M. E. Synthesis of Fe Oxide Core/Au Shell Nanoparticles by Iterative Hydroxylamine Seeding. *Nano Lett.* **2004**, *4*, 719–723.
55. Leopold, N.; Lendl, B. A New Method for Fast Preparation of Highly Surface-Enhanced Raman Scattering (SERS) Active Silver Colloids at Room Temperature by Reduction of Silver Nitrate with Hydroxylamine Hydrochloride. *J. Phys. Chem. B* **2003**, *107*, 5723–5727.
56. Nouh, E. S. A.; Roy, M.; Sarkar, S. Glucose Stabilized Magnetic Palladium Nanoparticles Exhibiting Enhanced Magnetic Properties Under Exposure to Hydrogen. *Mater. Express* **2012**, *2*, 275–284.
57. Lossen, W. Ueber Die Chlorhydrate Des Hydroxylamins. *Justus Liebigs Ann. Chem.* **1871**, *160*, 242–249.
58. Tschugaev, L. A.; Tschernjaev, I. I. LXXX.-Hydroxylamine Platinum Bases. *J. Chem. Soc., Trans.* **1918**, *113*, 884–897.
59. Zorbas-Seifried, S.; Jakupec, M. A.; Kukushkin, N. V.; Groessl, M.; Hartinger, C. G.; Semenova, O.; Zorbas, H.; Kukushkin, V. Y.; Keppler, B. K. Reversion of Structure-Activity Relationships of Antitumor Platinum Complexes by Acetoxime but Not Hydroxylamine Ligands. *Mol. Pharmacol.* **2007**, *71*, 357–365.
60. Zheng, H.; Smith, R. K.; Jun, Y.; Kisielowski, C.; Dahmen, U.; Alivisatos, A. P. Observation of Single Colloidal Platinum Nanocrystal Growth Trajectories. *Science* **2009**, *324*, 1309–1312.
61. Scherrer, P. Bestimmung der Grösse und der inneren Struktur von Kolloidteilchen mittels Röntgenstrahlen. *Nachr. Ges. Wiss. Goettingen, Math.-Phys. Kl.* **1918**, *2*, 98–100.
62. Wagner, C. D.; Muilenberg, G. E. *Handbook of X-Ray Photoelectron Spectroscopy: A Reference Book of Standard Data for Use in X-Ray Photoelectron Spectroscopy*; Physical Electronics Division, Perkin-Elmer Corp.: Eden Prairie, MN, 1979.

63. Wang, C.; Daimon, H.; Sun, S. Dumbbell-like Pt–Fe_3O_4 Nanoparticles and Their Enhanced Catalysis for Oxygen Reduction Reaction. *Nano Lett.* **2009**, *9*, 1493–1496.
64. Buck, M. R.; Bondi, J. F.; Schaak, R. E. A Total-Synthesis Framework for the Construction of High-Order Colloidal Hybrid Nanoparticles. *Nat. Chem.* **2012**, *4*, 37–44.
65. Lee, H.; Dellatore, S. M.; Miller, W. M.; Messersmith, P. B. Mussel-Inspired Surface Chemistry for Multifunctional Coatings. *Science* **2007**, *318*, 426–430.
66. Liu, Y.; Ai, K.; Lu, L. Polydopamine and Its Derivative Materials: Synthesis and Promising Applications in Energy, Environmental, and Biomedical Fields. *Chem. Rev.* **2014**, *114*, 5057–5115.
67. Ma, Y.; Zhang, X.; Zeng, T.; Cao, D.; Zhou, Z.; Li, W.; Niu, H.; Cai, Y. Polydopamine-Coated Magnetic Nanoparticles for Enrichment and Direct Detection of Small Molecule Pollutants Coupled with MALDI-TOF-MS. *ACS Appl. Mater. Interfaces* **2013**, *5*, 1024–1030.
68. Lin, L.-S.; Cong, Z.-X.; Cao, J.-B.; Ke, K.-M.; Peng, Q.-L.; Gao, J.; Yang, H.-H.; Liu, G.; Chen, X. Multifunctional Fe_3O_4@Polydopamine Core–Shell Nanocomposites for Intracellular mRNA Detection and Imaging-Guided Photothermal Therapy. *ACS Nano* **2014**, *8*, 3876–3883.
69. Willinger, M. G.; Zhang, W.; Bondarchuk, O.; Shaikhutdinov, S.; Freund, H.-J.; Schlögl, R. A Case of Strong Metal-Support Interactions: Combining Advanced Microscopy and Model Systems to Elucidate the Atomic Structure of Interfaces. *Angew. Chem., Int. Ed.* **2014**, *53*, 5998–6001.
70. Cullity, B. D.; Graham, C. D. *Introduction to Magnetic Materials*; John Wiley & Sons: New York, 2011.
71. Choi, K.; Ng, A. H. C.; Fobel, R.; Chang-Yen, D. A.; Yarnell, L. E.; Pearson, E. L.; Oleksak, C. M.; Fischer, A. T.; Luoma, R. P.; Robinson, J. M.; et al. Automated Digital Microfluidic Platform for Magnetic-Particle-Based Immunoassays with Optimization by Design of Experiments. *Anal. Chem.* **2013**, *85*, 9638–9646.
72. Park, J.; Hwang, K.; Park, Y.; Noh, J.-G.; Kim, H.-J.; Park, J.-Y.; Hwang, J.-H.; Hyeon, N.-M. Ultra-Large-Scale Syntheses of Monodisperse Nanocrystals. *Nat. Mater.* **2004**, *3*, 891–895.
73. Bard, A. J.; Faulkner, L. R. *Electrochemical Methods: Fundamentals and Applications*, 2nd ed.; Wiley: New York, 2001.
74. Xia, Y.; Whitesides, G. M. Soft Lithography. *Annu. Rev. Mater. Sci.* **1998**, *28*, 153–184.